Biophysical Journal, Volume *120*

Supplemental Information

Intestinal villus structure contributes to even shedding of epithelial cells

Yuto Kai

Supporting Material for Intestinal Villus Structure Contributes to Even Shedding of Epithelial Cells

Appendix S1: Derivation of the expected value and standard deviation of the shedding-cell ages

Let X be the stochastic variable representing the age when cells shed. First, the expected value of the shedding-cell age of the finger-like villus is given by

$$E(X) = \sum_{t=\tau_\mathrm{f}+1}^{\infty} t p_\mathrm{f} (1-p_\mathrm{f})^{t-\tau_\mathrm{f}-1}. \tag{S1}$$

By putting $k = t - \tau_\mathrm{f}$, we have

$$\begin{aligned} E(X) &= \sum_{k=1}^{\infty} (k+\tau_\mathrm{f}) p_\mathrm{f} (1-p_\mathrm{f})^{k-1} \\ &= p_\mathrm{f} \left[(1+\tau_\mathrm{f})(1-p_\mathrm{f})^0 + (2+\tau_\mathrm{f})(1-p_\mathrm{f})^1 + \cdots \right]. \end{aligned} \tag{S2}$$

Next, multiplying the both sides of Eq. S2 by $(1-p_\mathrm{f})$, we calculate

$$\begin{aligned} E(X) - (1-p_\mathrm{f})E(X) &= p_\mathrm{f} \left[\tau_\mathrm{f} + (1-p_\mathrm{f})^0 + (1-p_\mathrm{f})^1 + \cdots \right] \\ &= p_\mathrm{f} \left[\tau_\mathrm{f} + \frac{1}{1-(1-p_\mathrm{f})} \right]. \end{aligned} \tag{S3}$$

Finally, substituting $p_\mathrm{f} = n/(N - n\tau_\mathrm{f})$ from Eq. 5 into Eq. S3, the expected value is solved as

$$E(X) = \tau_\mathrm{f} + \frac{1}{p_\mathrm{f}} = \frac{N}{n} = T. \tag{S4}$$

To derive the standard deviation (SD) of the shedding-cell ages of the finger-like villus, we begin by calculating

$$E(X^2) = \sum_{t=\tau_\mathrm{f}+1}^{\infty} t^2 p_\mathrm{f} (1-p_\mathrm{f})^{t-\tau_\mathrm{f}-1}. \tag{S5}$$

Putting $k = t - \tau_\mathrm{f}$, we have

$$\begin{aligned} E(X^2) &= \sum_{k=1}^{\infty} (k+\tau_\mathrm{f})^2 p_\mathrm{f} (1-p_\mathrm{f})^{k-1} \\ &= p_\mathrm{f} \left[(1+\tau_\mathrm{f})^2 (1-p_\mathrm{f})^0 + (2+\tau_\mathrm{f})^2 (1-p_\mathrm{f})^1 + \cdots \right]. \end{aligned} \tag{S6}$$

Next, multiplying the both sides of Eq. S6 by $(1-p_\mathrm{f})$, we calculate

$$E(X^2) - (1-p_\mathrm{f})E(X^2) = p_\mathrm{f} \left[\{(1+\tau_\mathrm{f})^2 - 0^2\}(1-p_\mathrm{f})^0 + \{(2+\tau_\mathrm{f})^2 - (1+\tau_\mathrm{f})^2\}(1-p_\mathrm{f})^1 + \cdots \right], \tag{S7}$$

and get

$$E(X^2) = \tau_\mathrm{f}^2 + \left[(1+2\tau_\mathrm{f})(1-p_\mathrm{f})^0 + (3+2\tau_\mathrm{f})(1-p_\mathrm{f})^1 + \cdots \right]. \tag{S8}$$

Multiply the both sides of Eq. S8 by $(1-p_\mathrm{f})$ again, and we calculate

$$\begin{aligned} E(X^2) - (1-p_\mathrm{f})E(X^2) &= \tau_\mathrm{f}^2 - (1-p_\mathrm{f})\tau_\mathrm{f}^2 + \left[(1+2\tau_\mathrm{f})(1-p_\mathrm{f})^0 + 2(1-p_\mathrm{f})^1 + 2(1-p_\mathrm{f})^2 + \cdots \right] \\ &= p_\mathrm{f}\tau_\mathrm{f}^2 + \frac{2p_\mathrm{f}\tau_\mathrm{f} - p_\mathrm{f} + 2}{p_\mathrm{f}}, \end{aligned} \tag{S9}$$

and obtain

$$E(X^2) = \tau_\mathrm{f}^2 + \frac{2p_\mathrm{f}\tau_\mathrm{f} - p_\mathrm{f} + 2}{p_\mathrm{f}^2}. \tag{S10}$$

The variance of the shedding-cell ages is calculated from Eqs. S4 and S10 as

$$\begin{aligned} V(X) &= E(X^2) - [E(X)]^2 \\ &= \tau_{\mathrm{f}}^2 + \frac{2p_{\mathrm{f}}\tau_{\mathrm{f}} - p_{\mathrm{f}} + 2}{p_{\mathrm{f}}^2} - \left(\tau_{\mathrm{f}} + \frac{1}{p_{\mathrm{f}}}\right)^2 \\ &= \frac{1 - p_{\mathrm{f}}}{p_{\mathrm{f}}^2}, \end{aligned} \tag{S11}$$

thus the SD of the shedding-cell ages is given by

$$\sigma_{\mathrm{f}} = \frac{\sqrt{1 - p_{\mathrm{f}}}}{p_{\mathrm{f}}}. \tag{S12}$$

Finally, substituting $p_{\mathrm{f}} = n/(N - n\tau_{\mathrm{f}})$ from Eq. 5 into Eq. S12 and using $T = N/n$ from Eq. S4, we obtain

$$\sigma_{\mathrm{f}} = \sqrt{(T - \tau_{\mathrm{f}})(T - \tau_{\mathrm{f}} - 1)}. \tag{S13}$$

Appendix S2: Effects of the height of the finger-like villus

In this section, we examine how the height of the finger-like villus affects the spread of shedding-cell ages in the stochastic model. As shown in Fig. S1A, let r be the radius of the hemisphere and cylinder and h be the height of the cylinder of the finger-like structure. The length of the shortest path between the crypt orifices and the tip of the finger-like structure is

$$L_{\mathrm{f}} = \frac{1}{2}\pi r + h, \tag{S14}$$

and the epithelial surface area of the finger-like structure is

$$S_{\mathrm{f}} = 2\pi r^2 + 2\pi r h = 2\pi r(r + h). \tag{S15}$$

The cylinder base is not part of the epithelial surface area. From Eqs. S14 and S15, we obtain

$$L_{\mathrm{f}} = \frac{1}{4}\sqrt{2\pi S_{\mathrm{f}} + \pi^2 h^2} + \left(1 - \frac{\pi}{4}\right) h, \tag{S16}$$

and using Eq. S15, the overall height of the finger-like structure can be expressed in terms of its surface area as

$$H_{\mathrm{f}} = r + h = \frac{1}{2}\sqrt{\frac{2S_{\mathrm{f}}}{\pi} + h^2} + \frac{h}{2}. \tag{S17}$$

Thus, when S_{f} is constant, L_{f} increases as H_{f} increases via h, that is, the length of the shortest path between the crypt orifices and the villus tip lengthens as the overall height of the finger-like structure increases. Assuming that the cell migration speed is independent of the villus height, τ_{f} also increases as L_{f} increases. Assuming that the cell density is independent of the villus height, N is constant when the epithelial surface areas are the same. We also assume that n is the same regardless of the villus height. Therefore, although T is the same from Eq. S4, σ_{f} decreases as τ_{f} increases (Eq. S13) when $\tau_{\mathrm{f}} < T$ is established. A taller finger-like villus extends the length of the shortest path between the crypt orifices and the villus tip, and thereby delays the cell migration time over the shortest path, which reduces the spread of shedding-cell ages.

Appendix S3: Comparison of the finger-like and conical structures

In this section, we compare the spread of shedding-cell ages of the finger-like and conical structures using the stochastic model. First, we consider a right conical structure with the same epithelial surface area and radius as the finger-like structure as shown in Fig. S1B. The conical structure is assumed to be surrounded by crypts as with the finger-like structure, and cells move from the base and shed at the tip of the cone. Let r be its radius, l the slant height, and L_{co} the length of the shortest path of the conical structure, i.e., $L_{\mathrm{co}} = l$ (for a right circular cone). Considering an epithelial surface area of the conical structure equal to the finger-like structure, we obtain from Eq. S15

$$l = L_{\mathrm{co}} = \frac{S_{\mathrm{f}}}{\pi r} = 2(r + h). \tag{S18}$$

Here, the cone base is not part of the epithelial surface area. Again, h is the height of the cylinder of the finger-like structure. Then,

$$L_{\mathrm{co}} - L_{\mathrm{f}} = \left(2 - \frac{\pi}{2}\right) r + h > 0, \tag{S19}$$

that is, $L_{\mathrm{co}} > L_{\mathrm{f}}$ always holds regardless of r and h. We assume that the cell migration speed and cell density are independent of the shape of the structures, and that cell supply and shedding rates are constant regardless of the structures. Both structures hence have the same stochastic processes except for the shortest-path cell migration times. That is, both structures have the same values of N and n, but the conical structure has a longer shortest-path cell migration time than the finger-like structure. Finally, T is the same from Eq. S4, but the conical structure has a smaller SD of the shedding-cell ages than the finger-like structure from Eq. S13, under the condition that the conical structure's shortest-path cell migration time is smaller than T.

Appendix S4: Comparison of the finger-like, hemispheric, and circular disk structures

In this section, we first calculate the lengths of the shortest path between the crypt orifices and the shedding sites of the hemispheric and circular disk structures that have the same epithelial surface areas as the finger-like structure. We then compare the spread of shedding-cell ages among the finger-like, hemispheric, and circular disk structures using the stochastic model.

As shown in Fig. S1C, let ψ be the radius and L_{h} be the length of the shortest path of the hemispheric structure. As shown in Fig. S1D, let R be the radius and L_{c} be the length of the shortest path of the circular disk structure, where $R = L_{\mathrm{c}}$. Considering that both structures have the same epithelial surface area as the finger-like structure, each is expressed from Eq. S15 as

$$\psi = \sqrt{\frac{S_{\mathrm{f}}}{2\pi}} = \sqrt{r(r+h)}, \tag{S20}$$

$$L_{\mathrm{h}} = \frac{1}{2}\pi\psi = \frac{1}{2}\pi\sqrt{r(r+h)}, \tag{S21}$$

and

$$R = L_{\mathrm{c}} = \sqrt{\frac{S_{\mathrm{f}}}{\pi}} = \sqrt{2r(r+h)}. \tag{S22}$$

The base of the hemisphere does not contribute any epithelial surface area. We then compare the lengths of the shortest path among the three structures as follows:

$$L_{\mathrm{f}}^2 - L_{\mathrm{h}}^2 = \left(\pi - \frac{1}{4}\pi^2\right) rh + h^2 > 0, \tag{S23}$$

and

$$L_{\mathrm{h}}^2 - L_{\mathrm{c}}^2 = \left(\frac{1}{4}\pi^2 - 2\right) r^2 + \left(\frac{1}{4}\pi^2 - 2\right) rh > 0, \tag{S24}$$

that is, $L_{\mathrm{f}} > L_{\mathrm{h}} > L_{\mathrm{c}}$ always holds regardless of r and h. Again, we assume that the cell migration speed and cell density are independent of the shape of the structures, and that cell supply and shedding rates are constant regardless of the structures. The shortest cell migration time, therefore, decreases in the same order: $\tau_{\mathrm{f}} > \tau_{\mathrm{h}} > \tau_{\mathrm{c}}$, and all structures have the same values of N and n. The stochastic processes of all structures are the same except for the shortest-path cell migration times (Fig. 1), and the SDs of the shedding-cell ages of the hemispheric or circular disk structures are expressed by replacing τ_{f} of Eq. S13 with τ_{h} or τ_{c}. Finally, although T is the same among structures (Eq. S4), the finger-like structure has the least SDs of the shedding-cell ages, followed by the hemispheric and circular disk structures: $\sigma_{\mathrm{f}} < \sigma_{\mathrm{h}} < \sigma_{\mathrm{c}}$, when $\tau_{\mathrm{f}} < T$ is established. Here, σ_{h} and σ_{c} are the SDs of the shedding-cell ages of the hemispheric and circular disk structures.

Appendix S5: Derivation of the parameter values of the numerical calculation in the stochastic model

We estimate the parameter values of the numerical calculation in the stochastic model mainly based on the results of the experimental study of the murine intestinal villi by Krndija *et al.* (1). First, from a microscopic image of the side elevation of a finger-like villus shown in the study (1), we obtain the radius of the hemisphere and cylinder and height of the cylinder of the finger-like structure as $r = 50\mu$m and $h = 250\mu$m, respectively. We then estimate the length of the shortest path of the finger-like structure as $L_{\mathrm{f}} \sim 328.5\mu$m from Eq. S14 and the epithelial surface area of the finger-like structure as $S_{\mathrm{f}} \sim 94,248\mu\mathrm{m}^2$ from Eq. S15. Next, we

get the average cell density in the villus epithelium as $0.02/\mu\text{m}^2$ from the same villus image calculated by dividing the number of cells by the areas that cells occupy, and estimate the total number of cells in the finger-like structure's epithelial surface as $N = 94,248 \times 0.02 \sim 1,885$. Then, we obtain the average cell migration speed in the epithelium as 5μm/h as measured in the same study (1), and we estimate the shortest-path cell migration duration of the finger-like structure as $\tau_\text{f} = 328.5/5 \sim 65$ hours. Considering the discreteness of the stochastic model, the fractional part is truncated. Finally, the cell supply and shedding rates cannot be directly measured. It has been considered that cells ascend the villus over ~3 days (2), and we choose $n = 26$ hour^{-1} from Eq. S4 so that the average shedding-cell age becomes ~72 hours.

The lengths of the shortest path of the hemispheric and circular disk structures, with equal epithelial surface areas as the finger-like structure, are calculated as $L_\text{h} \sim 192.4\mu$m and $L_\text{c} \sim 173.2\mu$m from Eqs. S21 and S22, respectively. Assuming that both structures have the same average cell velocity as the finger-like structure, the shortest-path cell migration times are estimated as $\tau_\text{h} = 192.4/5 \sim 38$ hours and $\tau_\text{c} = 173.2/5 \sim 34$ hours, respectively. Next, assuming that both structures have the same average cell density in the epithelium as the finger-like structure, both structures also have $N = 1,885$ cells in their epithelial surfaces. In addition, we assume that both structures have the same cell supply and shedding rate $n = 26$ hour^{-1} as the finger-like structure. All structures, therefore, have the same total cell number $N = 1,885$ and cell supply and shedding rate $n = 26$ hour^{-1}, but different cell migration times of the shortest path: $\tau_\text{f} = 65$ hours, $\tau_\text{h} = 38$ hours, or $\tau_\text{c} = 34$ hours.

In the numerical calculation of the stochastic model, we proceed with the calculation loop as follows for each hour: n randomly-selected cells are removed as the shedding cells from those aged over the respective shortest-path cell migration times: τ_f, τ_h, or τ_c; remaining intraepithelial cells increment their age by one hour; we add n cells of age one hour in the epithelium. We put $N = 1,885$ cells of age one hour as an initial state. We run the simulation over 5,000 hours to attain a steady state, and then run for a further 15,000 hours. We obtain the data from the 15,000-hour calculation.

Appendix S6: Evaluation of the numerical calculation results in the stochastic model

In this section, we analytically calculate the SDs of the shedding-cell ages and the average intraepithelial-cell ages, and evaluate the results of the numerical calculation in the stochastic model.

Letting $T = N/n = 1,885/26 = 72.5$ hours from Eq. S4 and $\tau_\text{f} = 65$ hours in Eq. S13, we obtain $\sigma_\text{f} = 7$ hours. Similarly, $\sigma_\text{h} = 34$ hours and $\sigma_\text{c} = 38$ hours. These match the values of the numerical calculation as described in Fig. 2A.

Next, the average intraepithelial-cell age of the finger-like structure is given by

$$\frac{n}{N}\left[\sum_{t=1}^{\tau_\text{f}} t + \sum_{t=\tau_\text{f}+1}^{\infty} t(1-p_\text{f})^{t-\tau_\text{f}-1}\right]. \tag{S25}$$

Letting $N = 1,885$, $n = 26$ hour^{-1}, $\tau_\text{f} = 65$ hours, and $p_\text{f} = 2/15$ from Eq. 5 in Eq. S25, we obtain 37 hours. In the same way, we get 44.7 hours and 46.7 hours for the hemispheric and circular disk structures, respectively. These match the values of the numerical calculation as indicated by solid lines in Fig. 2B.

Appendix S7: Determination of the parameter values and dimensions in the cell-based models

In this section, we provide the determination of parameter values and dimensions in the 3D surface and 2D plane cell-based models. We conducted computational simulations of the cell-based models within Chaste, an open-source C++ library that provides a systematic framework for multi-cellular simulations (3). In both cell-based models, we proceed with the simulation loop as follows for each time step: neighboring cells are identified as having centers within the interaction distance; we calculate forces acting on each cell by Eq. 1; new cell locations are calculated by Eq. 3, and cells reach the shedding sites are removed; cell ages are updated and cell division occurs.

a 3D surface cell-based model

Figure S2 depicts the Villus, Bump and Disk models. All three structures have eight crypts of equal size arranged around regions with circular boundaries. The ratio of the radius to the height of the Villus is 1:5, which is equal to that used in the stochastic model. The Bump is hemispherical, and is wider and shorter than the Villus. In both structures, cells leaving the crypts enter the structures through a sloped base. In the Disk, cells leaving the crypts move directly onto the surface. In all structures, cells passing through the circular boundaries re-enter the regions from the center-symmetric positions to reduce the artificial accumulation of cells at the boundaries. All structures are scaled to have ~600 cells, of which ~150 are proliferating cells and ~450 are differentiated cells. The shedding sites are placed at heights of 14.9 cell diameters (CDs) and 7.535 CDs from the crypt orifices of the Villus and Bump, respectively. The Disk's shedding site, 1.4 CDs in diameter, is at its center. These shedding sites are determined to have

equal perimeters and to provide similar cell-shedding behavior among structures. The length of the shortest path between the crypt orifices and the shedding sites is shorter 17.9 CDs on the Villus, 11.9 CDs on the Bump, and 9.1 CDs on the Disk.

We use spring constant $\mu = 30$ and drag coefficient $\eta = 1.0$ for all structures (3) and confirmed that cells ascend sides of the Villus with little rearrangements (Movie S1). We set 1.5 CDs as the interaction distance between neighboring cells and 1/120 cell hour as the time step Δt (3). The division interval of each proliferative cell is drawn from a truncated normal distribution with mean 10 cell hours, standard deviation 100, and lower band 10 cell hours to ensure that cell division does not artificially synchronize and so the total cell number fluctuates by no more than 5% for all structures (Fig. S3A). All structures are set to have approximately equal numbers of proliferative cells and similar division intervals, with approximately the same proliferation rates among the structures, confirmed by the approximately equal average cell-shedding rates among structures (Fig. 3B). We summarize the parameter values used in the 3D model in Table S1.

In the 3D model simulations, proliferative cells are placed in the crypt surfaces as an initial state. We first calculate 2,000 cell hours to establish until steady-state conditions, and then run further 14,000 cell hours, which is repeated twice. The shedding-cell ages and differentiated-cell ages were obtained for each cell hour. We combine the results of twice-repeated simulations at steady state and obtain data.

b 2D plane cell-based model

In the 2D plane cell-based model, the cell interaction neighborhood radius is 1.5 CDs and the time step Δt is 1/120 cell hour. As normal settings, we use spring constant $\mu = 30$ and drag coefficient $\eta = 1.0$ as in the 3D model. The Long and Short models are depicted in Fig. S4A. Their dimensions are determined based on the "normal" settings that we use in the results of Fig. 4. Both have one crypt and one shedding site, and the widths of the crypt and that of the shedding site are equal between them. We determine the widths and lengths of the shapes based on a cell arrangement where cells are connected by springs of natural length as shown in Fig. S4B. The spacing between cell columns is $\sqrt{3}/2$ CDs as indicated by the red arrow, and we set the width of $7 \times \sqrt{3}/2 \sim 6.06$ CDs for the Long and that of $9 \times \sqrt{3}/2 \sim 7.79$ CDs for the Short so that 8 and 10 cell columns fit within their widths, respectively. We then set the lengths of shapes as indicated by green dotted lines in Fig. S4A for a total cell number of ~200. The crypts and the shedding sites are tapered to the transport regions by straight lines with slopes of ±0.5, which come from the lines connecting adjacent cell centers as indicated by the dotted red lines in Fig. S4B. These taperings are useful for making the influences of the shapes of the Long and Short on cell behavior roughly the same. To reduce artificial cell movement along the boundaries, the periodic boundary condition is imposed on the left- and right-hand sides, as indicated by the red lines of Fig. S4A: cells passing through one side re-enter the regions through the opposite side. Other black lines have the reflective boundary condition. Finally, we confirmed that collective cell migration with little cell rearrangement is achieved in the upper regions of both shapes under the normal settings (Fig. 4A and Movie S2).

We select the cell proliferation rates so that cell shed smoothly and so that fluctuations in the total cell number are below 5% for both shapes (Fig. S4C). The cell proliferation rate is defined by the proliferative-cell number and cell-division interval. For both shapes, the division interval of each proliferative cell is drawn from a truncated normal distribution with mean 8 cell hours, standard deviation 3, and lower band 8 cell hours, which is chosen to ensure that cell division does not artificially synchronize. Next, the Short requires a slightly longer crypt depth (D) to have approximately equal proliferative-cell numbers as the Long, as shown in Table S2, because the Short has a lower average cell density than the Long (Fig. S4D).

In the 2D model, we also examine two cases: active cell migration and different material properties of cells.

Active cell migration. We vary α between 0 and 0.2 where cell proliferation rates and cell-shedding rates can be balanced. We use the parameter values of the normal condition except for D.

Different material properties of cells. We fix $\eta = 1.0$ and vary μ between 10 and 50. We use the parameter values of the normal condition except for μ and D.

In both cases, we use the same model shapes except for D (Fig. S4A). For consistency, we set approximately equal cell proliferation rates for all conditions. To accomplish this, we need to set approximately equal division intervals and proliferative-cell numbers among different conditions. The proliferative-cell density in the crypts also varies because the average cell density varied with the parameter values (Figs. 5C and 6C). We hence regulated D so that all conditions have ~15 proliferative cells in each crypt as shown in Table S2. Finally, all conditions show approximately equal average cell-shedding rates (Figs. 5A and 6A), which ensures approximately equal cell proliferation rates among different conditions.

In the simulations of the 2D model, proliferative cells are placed in the crypt surfaces as an initial state. we first calculate for 1,000 cell hours to establish a steady state, and then run for a further 7,000 cell hours, which is repeated two times. The shedding-cell ages and differentiated-cell ages were obtained for each cell hour. We combine the results of twice-repeated simulations at steady state and obtain data.

Calculation of cell density

In both cell-based models, we divide respective average number of differentiated cells by the surface areas subtracting the crypt surface areas to obtain the average cell density.

In the 3D model, we obtain average cell density profiles of the Villus and Disk as follows: the cylindrical part of the Villus and Disk are divided into five regions as indicated by the dotted red and blue lines as shown in Fig. S2; we divide the average cell number of each region by its surface area; we calculate rescaled average cell density of each region relative to region one.

In the 2D model, we get average cell density profiles of the Long and Short as follows: each model is divided into five regions indicated by the dotted purple and cyan lines as shown in Fig. S4A; the average cell number of each region is divided by its surface area; we calculate rescaled average cell density of each region relative to region one.

Appendix S8: Simulation of the Narrow shape in the 2D plane cell-based model

In this section, we examine whether the width of the model affects the separation of cell population movement for a small value of λ (= 10). We then built a shape with the same length as the Long model but a narrower width, as shown in Fig. S6Ei. The width is chosen so that the average total cell number is ~200 when λ = 10 (Fig. S6Eii); other geometrical parameters are the same as in Fig. S4A. We regulate D and set an equal cell proliferation rate to the normal condition (Table S2), and the average cell-shedding rate becomes approximately the same as the normal (Fig. S6Eiii). Cells move slowly with little cell mixing in the narrow shape (Movie S5), and gradual cell age distribution is shown on the surface (Fig. S6Eiv). As shown in Fig. S6Ev, the narrow shape exhibits a unimodal shedding-cell age distribution, indicating that the separation of population movement does not occur in the narrow channel. Wider channels, therefore, lead the separation of cell population movement, and the threshold width of the separation would depend on the magnitude of λ.

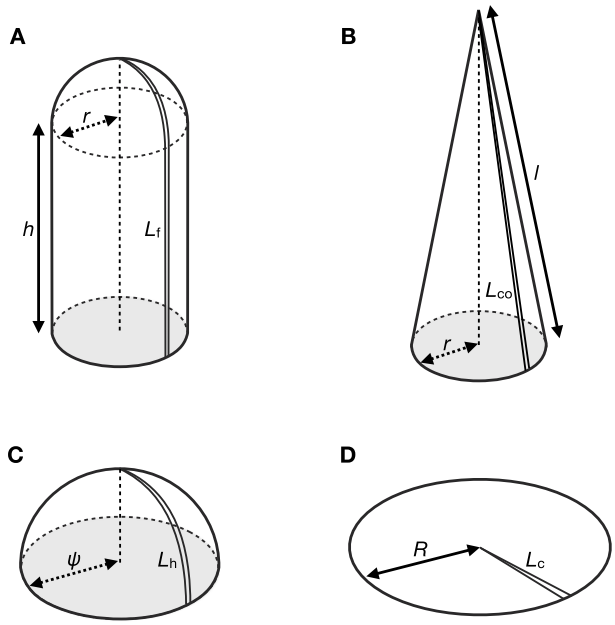

Figure S1: Four structures considered in the stochastic model: the finger-like (A), conical (B), hemispheric (C), and circular disk structures (D). The finger-like, conical, and hemispheric structures do not have their bases that are colored gray: base areas of these structures are not included in the respective epithelial surface areas. (A) The finger-like structure comprises a hemisphere with radius r coupled to a cylinder with radius r and height h. L_f is the length of the shortest path between the crypt orifices and the tip of the finger-like structure. (B) Shown is the conical structure (a right circular cone) with radius r and slant height l. L_{co} is the length of the shortest path between the crypt orifices and the tip of the cone; L_{co} is equal to l. (C) Given is the hemispheric structure with radius ψ. L_h is the length of the shortest path between the crypt orifices and the tip of the hemisphere. (D) Shown is the circular disk structure with radius R. L_c is the length of the shortest path between the crypt orifices and the center of the circle; L_c is equal to R.

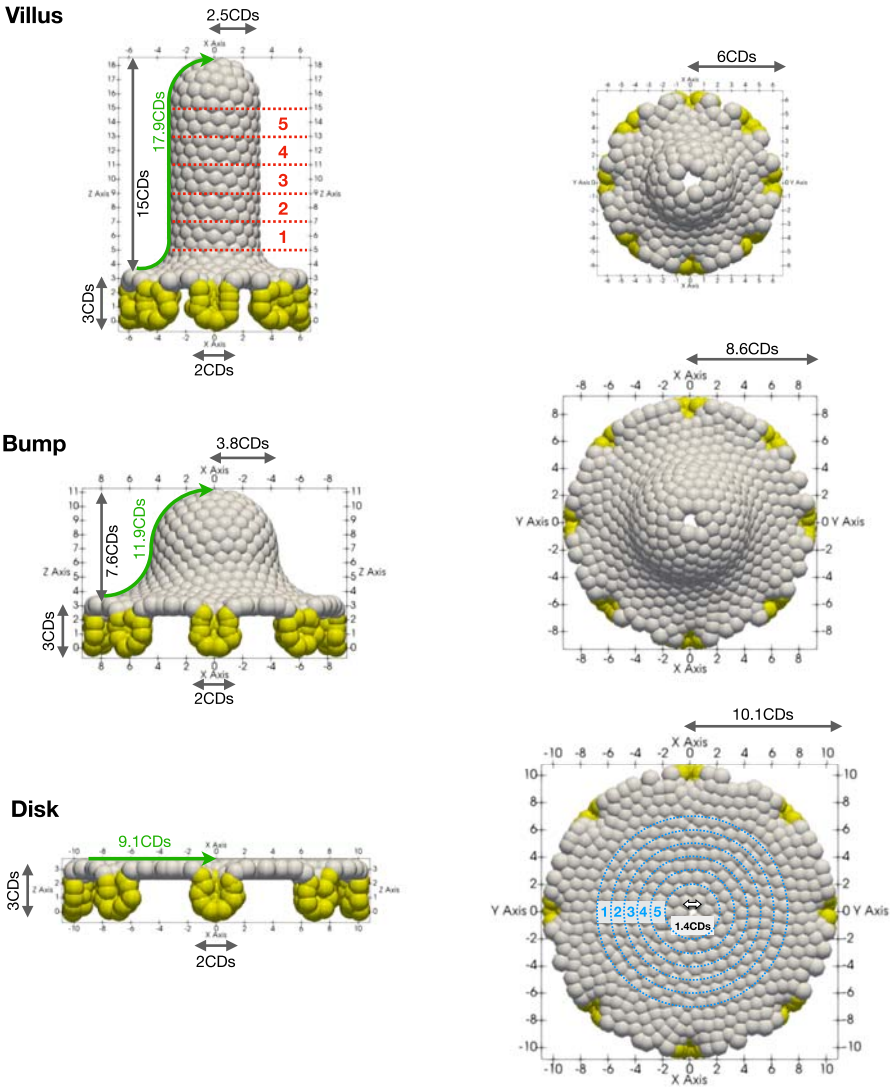

Figure S2: 3D surface cell-based models: Villus (*top*), Bump (*middle*), and Disk (*bottom*). The spatial units are cell diameters (CDs). The left panels are the side elevations and the right panels are the top-down plan views. Proliferative cells are colored yellow; differentiated cells are colored white. Holes seen in the plan views are shedding sites. Green arrows on the elevations show the shortest paths between the crypt orifices and the shedding sites. The red and blue numbers of the Villus and Disk indicate zones for calculating local average cell density.

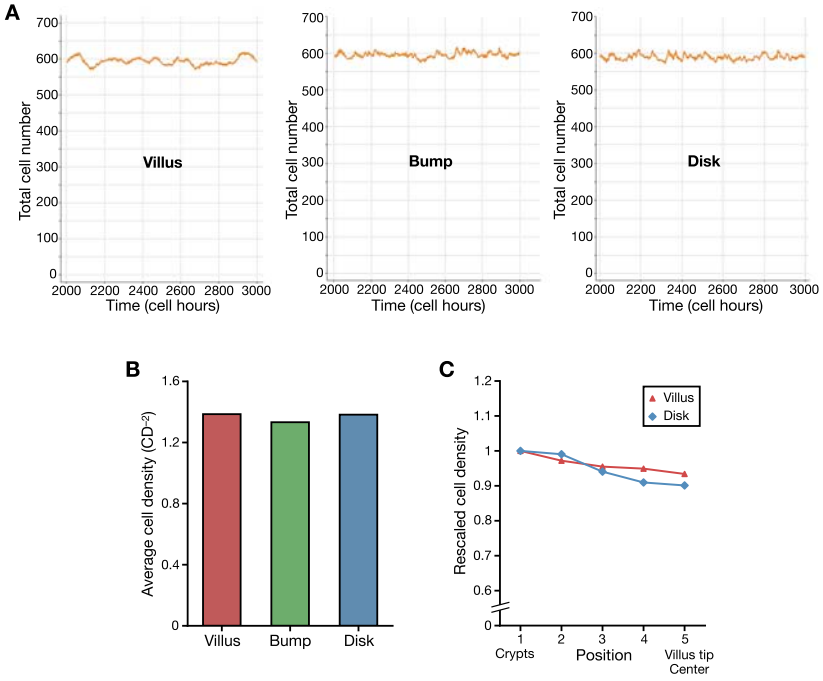

Figure S3: 3D surface cell-based model results. (A) Given are the total cell numbers at steady state of the Villus (*left*), Bump (*middle*), and Disk (*right*). (B) Given is the average cell density. (C) Given are the rescaled average cell density profiles along the crypt–villus tip (Villus) or crypt–center (Disk) axes. Each position number corresponds to a divided zone as shown in Fig. S2.

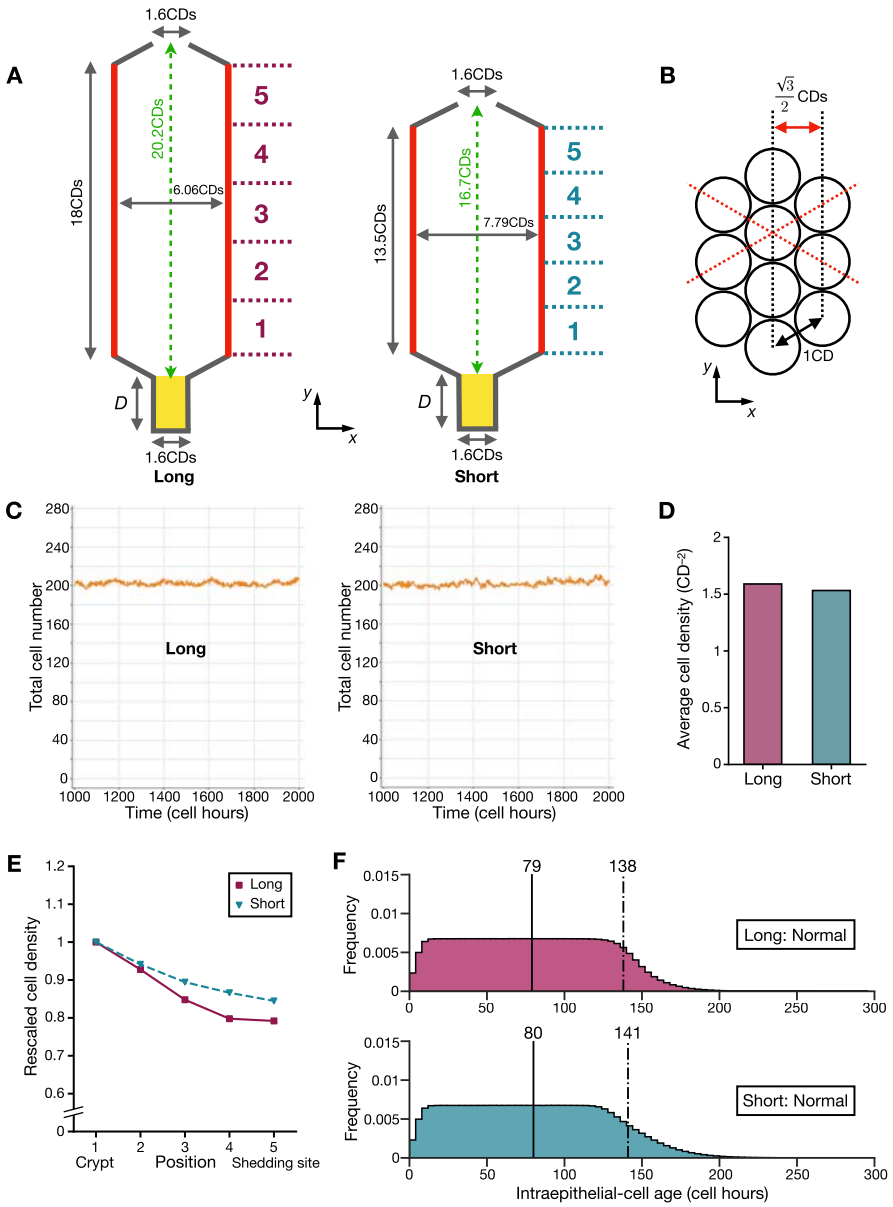

Figure S4: 2D plane cell-based model. (A) Given are the schematic outlines of the 2D models: Long (*left*) and Short (*right*). The crypt areas are colored yellow. D is the crypt depth, regulated to achieve equal cell proliferation rates among different conditions. Periodicity in the x-axis direction is applied at the red lines, and the reflective condition is applied to other black lines. The green arrows indicate the distances between the crypt orifices and the shedding sites. The purple and cyan numbers indicate zones for calculating local average cell density. (B) Shown is an arrangement of cells connected by springs of natural length. Each circle represents a cell. The red arrow represents the spacing between cell columns. Red dotted lines connect adjacent cell centers. (C–F) The results of the normal condition are shown. (C) Given are the total number of cells at steady state of the Long (*left*) and Short (*right*). (D) Shown is the average cell density. (E) Given are the rescaled average cell density profiles along the crypt–shedding site axis. Each position number corresponds to the same number of divided regions of Fig. S4A. (F) Shown are the intraepithelial-cell age distributions of the Long (*top*) and Short (*bottom*). The decreased frequency around age zero is because proliferative cells constitute the majority. The solid lines represent the average intraepithelial-cell ages, the dot–dash lines represent the old intraepithelial-cell age as indicated by the 90th percentile.

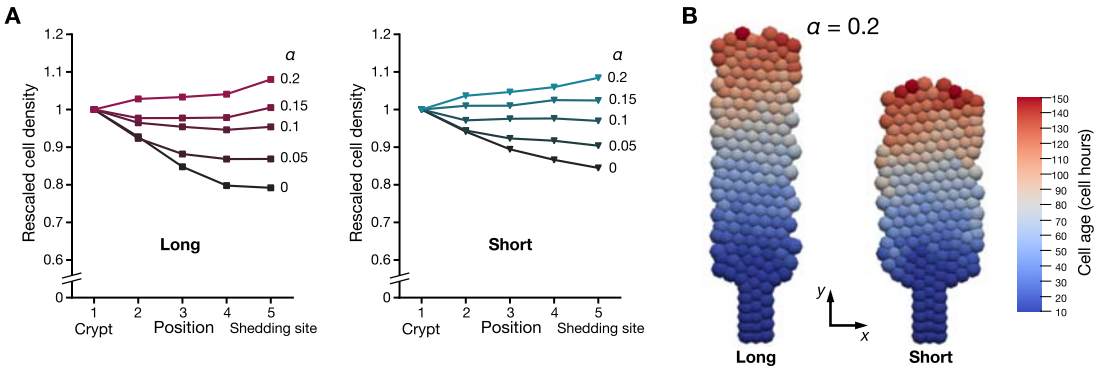

Figure S5: Effects of active cell migration. (A) Given are the rescaled average cell density profiles along the crypt–shedding site axis for various applied force magnitudes α of the Long (*left*) and Short (*right*). Each position number corresponds to the same number of divided regions of Fig. S4A. (B) Shown are cell age distributions in the surfaces at steady state for $\alpha = 0.2$ of the Long (*left*) and Short (*right*). Both shapes have the same color scale.

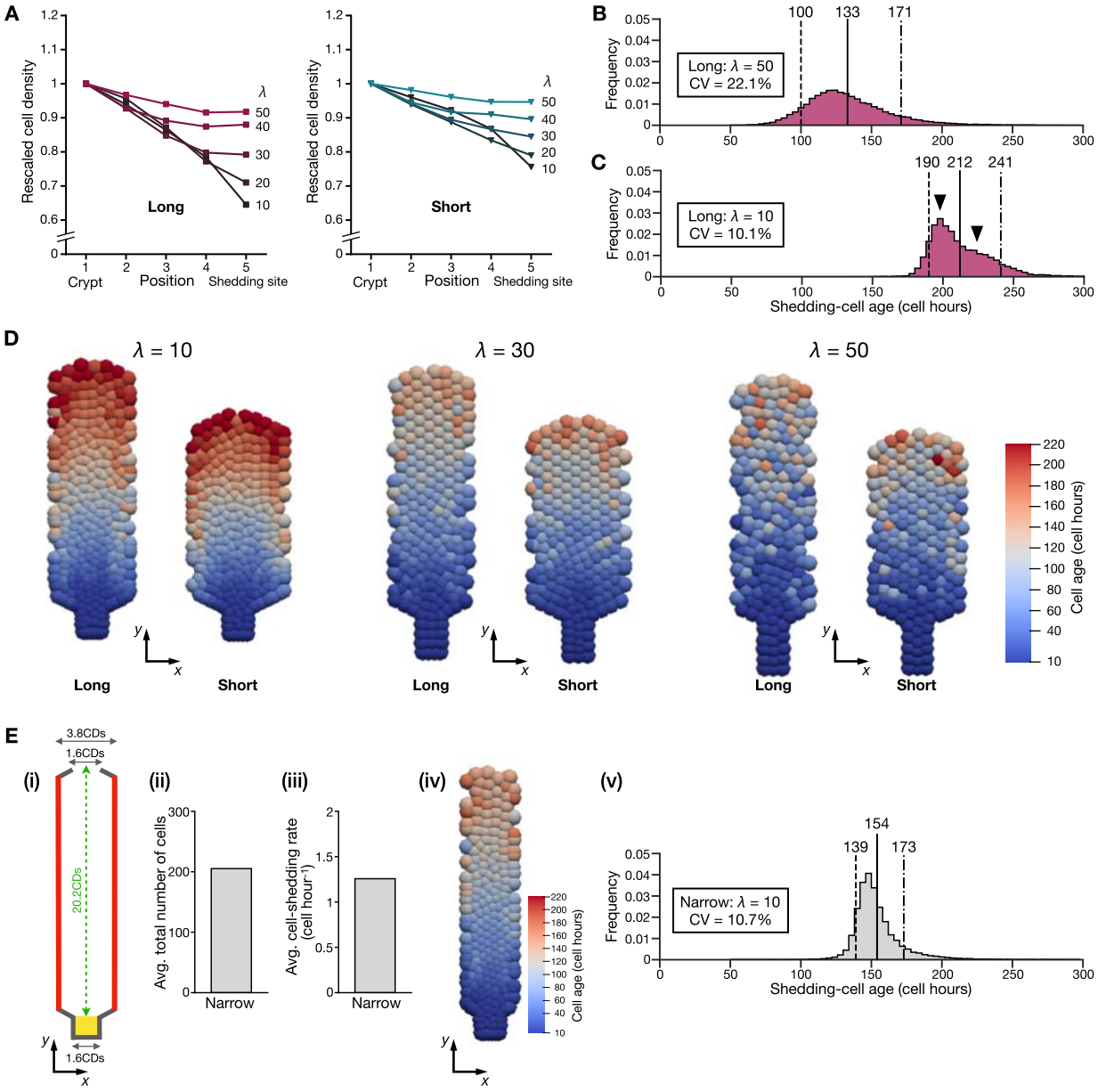

Figure S6: Effects of different material properties of cells. (A) Given are the rescaled average cell density profiles along the crypt–shedding site axis for various λ of the Long (*left*) and Short (*right*). Each position number corresponds to the same number of divided regions of Fig. S4A. (B, C) Shown are the shedding-cell age distributions of Long for $\lambda = 50$ (B), and $\lambda = 10$ (C). The dashed lines represent the early shedding-cell ages as indicated by 10th percentile of the shedding-cell ages, the solid lines represent the average shedding-cell ages, and the dot–dashed lines represent the late shedding-cell ages as indicated by the 90th percentile of the shedding-cell ages. Arrowheads indicate distribution bimodality. (D) Given are cell age distributions in the surfaces of the Long and Short at steady state for $\lambda = 10$ (*left panels*), $\lambda = 30$: the normal condition (*middle panels*), and $\lambda = 50$ (*right panels*). All conditions have the same color scale. (E) The results of the Narrow shape for $\lambda = 10$ are given. (i) Shown is the schematic of the Narrow shape; the crypt area is colored yellow, periodicity in the x-axis direction is applied at the red lines, and the reflective condition is applied to other black lines. The green arrow indicates the distance between the crypt orifice and the shedding site. (ii) Given is the average total number of cells in the model. (iii) Given is the average number of cells that shed per one cell hour. (iv) Given is the cell age distribution in the surface. (v) Given is the shedding-cell age distribution. The dashed line represents the early shedding-cell age, the solid line represents the average shedding-cell age, and the dot–dashed line represents the late shedding-cell age.

Supporting Movie Legends

Movie S1:
A movie showing the 3D surface cell-based model: Villus, Bump, and Disk.

Movie S2:
A movie showing the normal condition in the 2D plane cell-based model: Long and Short.

Movie S3:
A movie of active cell migration in the 2D plane cell-based model: Long and Short for $\alpha = 0.2$.

Movie S4:
A movie comparing different material properties of cells in the 2D plane cell-based model: Long and Short for $\lambda = 10$ (*left panels*), and Long and Short for $\lambda = 50$ (*right panels*).

Movie S5:
A movie showing the Narrow 2D plane cell-based model with $\lambda = 10$.

In all movies, proliferative cells are colored yellow and differentiated cells are colored white.

Table S1: Parameter Values in the 3D Surface Cell-Based Model

	μ	η
Villus	30	1.0
Bump	30	1.0
Disk	30	1.0

μ: connecting spring constant.
η: drag coefficient.

Table S2: Parameter Values in the 2D Plane Cell-Based Model

	Shape	μ	η	α	D (CD)
Normal condition	Long$^\sharp$	30	1.0	0	3.25
	Short$^\flat$	30	1.0	0	3.3
Active cell migration	Long$^\sharp$	30	1.0	0	3.25
	Short$^\flat$	30	1.0	0	3.3
	Long	30	1.0	0.05	3.45
	Short	30	1.0	0.05	3.45
	Long	30	1.0	0.1	3.63
	Short	30	1.0	0.1	3.6
	Long	30	1.0	0.15	4.0
	Short	30	1.0	0.15	3.9
	Long	30	1.0	0.2	4.25
	Short	30	1.0	0.2	4.15
Different material properties of cells	Long	10	1.0	0	1.95
	Short	10	1.0	0	2.15
	Long	20	1.0	0	2.8
	Short	20	1.0	0	2.9
	Long$^\sharp$	30	1.0	0	3.25
	Short$^\flat$	30	1.0	0	3.3
	Long	40	1.0	0	3.7
	Short	40	1.0	0	3.7
	Long	50	1.0	0	4.1
	Short	50	1.0	0	4.1
	Narrow	10	1.0	0	1.78

μ: connecting spring constant.
η: drag coefficient.
α: magnitude of the active cell migration force.
D: depth of the crypt.
$\sharp$: the same as Long of the normal condition.
$\flat$: the same as Short of the normal condition.

Supporting References

1. Krndija, D., F. El Marjou, B. Guirao, S. Richon, O. Leroy, Y. Bellaiche, E. Hannezo, and D. M. Vignjevic, 2019. Active cell migration is critical for steady-state epithelial turnover in the gut. *Science* 365:705–710.

2. Darwich, A. S., U. Aslam, D. M. Ashcroft, and A. Rostami-Hodjegan, 2014. Meta-analysis of the turnover of intestinal epithelia in preclinical animal species and humans. *Drug Metab. Dispos.* 42:2016–2022.

3. Mirams, G. R., C. J. Arthurs, M. O. Bernabeu, R. Bordas, J. Cooper, A. Corrias, Y. Davit, S. J. Dunn, A. G. Fletcher, D. G. Harvey, M. E. Marsh, J. M. Osborne, P. Pathmanathan, J. Pitt-Francis, J. Southern, N. Zemzemi, and D. J. Gavaghan, 2013. Chaste: an open source C++ library for computational physiology and biology. *PLoS Comput. Biol.* 9:e1002970.